Journal of Manufacturing Processes 121 (2024) 205–220

Contents lists available at ScienceDirect

Journal of Manufacturing Processes

journal homepage: www.elsevier.com/locate/manpro

Integrated modeling for residual stress and failure behavior in welded Grade 91 steel cladded with nickel alloy

Xuesong Gao [a], Abdelrahman Abdelmotagaly [b], Timothy Pickle [b], Aric Adamson [b], Chad Augustine [c], Zhenzhen Yu [b], Wei Zhang [a,*]

[a] Department of Materials Science and Engineering, The Ohio State University, 1248 Arthur E Adams Dr, Columbus, OH 43221, United States
[b] Department of Metallurgical and Materials Engineering, Colorado School of Mines, 1500 Illinois St, Golden, CO 80401, United States
[c] National Renewable Energy Laboratory, 15013 Denver W Pkwy, Golden, CO 80401, United States

ARTICLE INFO

Keywords:
Bimetallic materials
Grade 91 steel
Integrated modeling
Fracture
Austenite-martensite transformation
Residual stress and distortion

ABSTRACT

Grade 91 (G91) steel cladded with nickel alloy C22 presents a promising material solution for the Generation 3 concentrating solar power systems. Failure behavior for weld joints of such bimetallic material is complex and affected by many factors. Currently, numerical models considering both welding and loading of bimetallic materials are lacking in the literature. This study introduces an integrated model, encompassing welding, post-weld heat treatment (PWHT), and tensile testing to investigate the fracture behavior of a welded bimetallic plate with G91 steel substrate and alloy C22 clad. The welding and PWHT analyses consider incomplete austenite-martensite transformations and creep, respectively, in the calculation of residual stress and distortion. The tensile testing analysis assesses the fracture behavior of the weld joint, accounting for the effect of residual stress and material inhomogeneity. The simulation results of fusion zone shapes, welding-induced distortion, soft regions in heat-affected zone, and local strains during tensile testing are compared to the respective experimental data. It has been found that PWHT effectively mitigates the residual stress in the weld metal but introduces tensile stress in the clad and a high stress gradient at the bonding interface. The residual stress after PWHT has an insignificant effect on the G91/C22 weld failure during tensile testing. Instead, the fracture location is primarily dictated by the relative strength between the base and weld metals. However, the high stress gradient at the clad-substrate interface results in a large triaxiality factor, potentially contributing to the debonding in cases of weak bonding strength.

1. Introduction

Subcomponents (e.g., pipes) in Generation 3 concentrating solar power systems (Gen3 CSP) are designed for service in high temperature and corrosive conditions [1]. Fabricating these subcomponents out of nickel alloys such as H282 can be very expensive. A cost-effective alternative is to use bimetallic material comprising a low-cost substrate to provide the required high-temperature strength that is cladded with a high-cost alloy for corrosion resistance. One such promising bimetallic material is Grade 91 (G91) steel cladded with nickel alloy C22 (abbreviated as G91/C22). Specifically, G91 steel, commonly designed as 9Cr-1Mo-V, is widely used for high-temperature service in the fossil and nuclear power generation industry [2,3]. C22 is a nickel-chromium-molybdenum solid solution-strengthened alloy with excellent corrosion and oxidation resistance as well as good mechanical properties at high temperatures [4].

The fracture behavior of bimetallic materials is complicated due to the inhomogeneous microstructures and mechanical properties, particularly at the bonding interface. The interface tends to be the location of fracture initiation and may be separated before the final fracture [5,6]. Li et al. [7] studied the fracture behavior of carbon steel plate cladded with stainless steel (SS) during uniaxial tensile testing. The presence of a relatively stronger clad introduces a stress discontinuity at the interface, leading to shear stress accumulation and fracture initiation at the interface. On the other hand, cracking can also occur on the substrate surface and propagate to the interface when the clad material is highly ductile [8,9]. The thickness ratio of the clad material to the substrate, namely the clad ratio, also influences the fracture behavior by governing the mechanical properties of the composite material in either linear or non-linear manners [10].

* Corresponding author.
E-mail address: zhang.3978@osu.edu (W. Zhang).

https://doi.org/10.1016/j.jmapro.2024.05.036
Received 20 March 2024; Received in revised form 29 April 2024; Accepted 15 May 2024
Available online 21 May 2024

Welding and post-weld heat treatment (PWHT) add additional complexity to the fracture behavior of bimetallic materials. Specifically, temperature gradients and phase transformations during welding lead to residual stress, stress concentration and inhomogeneous microstructure in the weld [11]. PWHT typically alleviates the inhomogeneity in microstructure and mechanical properties of weld joints [12,13]. However, for bimetallic materials, new residual stress can be introduced due to the different physical and mechanical properties, such as the coefficient of thermal expansion (CTE) between the substrate and clad materials. Such CTE mismatch would cause a tensile residual stress in the material with a higher CTE, a compressive residual stress in the other material, and a high stress gradient at the bonding interface [14,15].

It has been found various factors related to the materials [16,17], processing parameters [18], and welding techniques [19,20] can affect the fracture location being in the fusion zone (FZ), heat-affected zone (HAZ) or base metal in a bimetallic material weld. For example, in the case of bimetallic plates of X65 pipeline steel substrate cladded with duplex stainless steel (DSS) 2205 without a weld, the fracture strain in tensile testing has a uniform distribution across the two materials [19]. However, in laser-welded joints of this bimetallic plate, the fracture strain is initially localized in the FZ of DSS 2205 before propagating towards the base metal of X65 [19]. In a subsequent study by the same authors, fracture initiation occurs at the HAZ of the DSS 2205 clad and progresses towards the base metal of X65 in weldments joined by multi-pass gas metal arc welding [20]. This difference in fracture location is rationalized by the distinct microstructures and the associated mechanical strengths resulting from laser versus gas metal arc welding processes. In contrast, the fracture location for weld joints of 10CrNi3-MoV steel substrate cladded with SS 304 L is observed at the base metal of the SS clad. It is attributed to the strengthening of FZ and HAZ of the steel substrate due to the formation of carbides, vanadium-containing phases, and a high dislocation density [21]. Additionally, fracture locations in the base metal of the substrate are also reported in the literature [22,23].

Given the large number of factors that can potentially influence the fracture behavior of weld joints of bimetallic materials, it is desirable to develop a numerical model for welding and loading of bimetallic materials. Such a model is currently lacking in the literature. This study introduces an integrated model, encompassing welding, PWHT, and tensile testing, to comprehensively investigate the fracture behavior of G91/C22 weld joints. Specifically, the welding analysis evaluates residual stress and distortion in a double-sided multi-pass configuration, taking into account the incomplete austenite-martensite transformations. Furthermore, the redistribution of residual stress during PWHT is examined, accounting for creep and thermal strain mismatch between the substrate and clad materials. The failure behavior of the G91/C22 weld joints is assessed by the tensile testing analysis, which incorporates the residual stress and material inhomogeneity from welding and PWHT.

2. Experimental approaches

As-received G91 plate in a tempered condition with a thickness of 19 mm was first cladded with nickel alloy C22 plate with a thickness of 3 mm by explosive welding. The G91/C22 clad plate of 520 × 300 × 22 mm was used for weld joint fabrication. The weld bead arrangement is shown in Fig. 1a, where the G91 substrate passes were completed first followed by the C22 clad passes. Flux-cored arc welding (FCAW) with E91T1-B9-H4 filler wire was used for the substrate, and pulsed gas metal arc welding (GMAW) with Oxford Alloy 622 filler wire was used for the clad. The plate was preheated to 511 K, and the maximum inter-pass temperature was maintained below 572 K for all weld passes. The average travel speed was 7.6 mm/s, the welding current ranged between 150 A and 200 A, the wire feeding speed ranged from 110 to 120 mm/s, the voltage was maintained at 25 V, and the shielding gas was Ar + 25 % CO_2 for the substrate passes. For the clad passes, the average travel

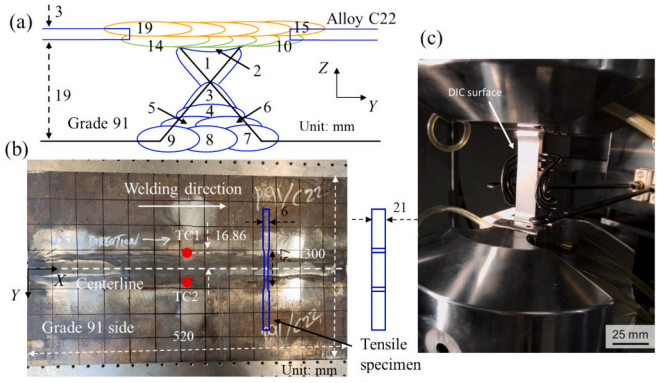

Fig. 1. (a) G91/C22 weld bead setup, (b) G91/C22 weldment after post-weld heat treatment, and (c) the setup for room temperature tensile testing with DIC to measure the strain map. Positions of thermocouples were denoted by red points, and the tensile test sample extraction is highlighted by blue lines in (b). Note that the induction coil for high-temperature testing was not used in this study. (For interpretation of the references to colour in this figure legend, the reader is referred to the web version of this article.)

speed is the same as that for the substrate passes but the welding current ranged from 130 to 160 A, and the shielding gas was changed to Ar + 25 % He. A multi-step schedule was used for PWHT. Above 700 K (427 °C), the sample was heated at a maximum rate of 204 K/h to the PWHT temperature of 1005 K (732 °C). It was soaked at this temperature for 2 h and then cooled down at a controlled rate of 260 K/h to 700 K. The heating and cooling rates were uncontrolled below 700 K.

The post-weld heat treated weldment is shown in Fig. 1b, where the red points (designated as TC1 and TC2) represent the locations of the thermocouples employed to record the inter-pass temperatures during welding. The grid on the weldment surface, consisting of 40 mm × 40 mm squares, was used to measure the out-of-the-plane distortion at each line intersection. Fig. 1b also shows an example of tensile sample extraction from the weldment where the size and location of the tensile sample is marked by blue lines. Specifically, tensile specimens had the following dimensions: 57 mm gauge length, 6 mm thickness, and 21 mm width which are aligned to the weldment's width, length and thickness directions, respectively. Room temperature (RT) tensile tests were carried out using a hydraulic MTS Landmark 370.10 universal testing machine with a quasi-static 10^{-3}/s strain rate. During tensile testing, the digital image correlation (DIC) method was employed to measure the strain distribution on the surface containing a weld transverse cross-section, as shown in Fig. 1c.

Vicker's microhardness map was measured on the weld transverse cross-section with a vertical spacing (parallel to thickness direction) of 1.15 mm and a horizontal spacing of 0.5 mm, using a 500-g-force load. Assuming symmetry across the centerline of the weld, the microhardness map was measured only on one half of the weld cross-section.

3. Modeling approaches

Given the complexities of modeling explosive welding process, a main simplification is that the residual stress and microstructural change introduced by explosive cladding is not considered. This simplification is somewhat justified as such residual stress and microstructural change are very localized to the bonding interface [24]. Deng et al. [25,26] showed that the residual stress in the weld zone can be accurately captured even without considering the pre-welding steps such as cladding. Additionally, dilution due to mixing among nickel alloy clad, G91 steel substrate, and the two different filler wires is ignored. The integrated process-performance modeling thus consists of a welding process model, a PWHT model, and a tensile testing model. A description of these models and their integration is provided as follows.

3.1. Welding process model

The process model is based on the widely used sequentially-coupled thermo-metallurgical-structure analysis approach in the literature. Specifically, the welding thermal analysis solves the transient heat conduction equation to determine the temperature field. The calculated thermal histories are then applied as thermal loads to the welding metallurgical-structure analysis, which determines the displacement, strain, and stress fields by solving the static equilibrium equations. The austenite-martensite transformations are considered by the metallurgical analysis, and the resultant fractions of each phase are used to calculate the yield strength and phase transformation strain (to be discussed in Section 3.2).

The thermal model is constructed based on the experimental weld macrograph shown in Fig. 2a, where the fusion lines of the 19 individual beads are marked by dashed lines. The weld was cut into two halves along the vertical centerline due to the large size. Fig. 2b shows the meshed transverse cross-section corresponding to the experimental weld macrograph. This cross-section was extruded along the weld seam direction (X) to create a 3D mesh, as shown in Fig. 2c. The meshed plate, 260 mm long × 300 mm wide × 22 mm thick, comprised a center region with fine elements and two outer regions with coarse elements. Specifically, the center region, with a width of 60 mm to encompass the FZs and the adjacent HAZs, was meshed with elements ranging from 1 to 3 mm in size. The two outer regions were meshed with gradually coarsening elements further away from the weld center with sizes ranging from 3 to 15 mm. A tie constraint was used between the center and the outer regions to handle the mesh transition at the interfaces. Note that the model geometry was half of the experimental specimen in the length direction to further reduce the computational cost. Additionally, a shorter geometry with a length of 100 mm was also examined. The comparison between the two reduced-geometry models shows that the length of the geometry used in the model has an insignificant effect on the predicted stress and distortion results for the relatively stiff plates considered in this study.

In the welding thermal analysis, the initial temperature was 511 K, and a typical Goldak heat flux was employed with parameters calibrated against the fusion boundaries of individual beads. Coefficients for convective heat transfer and radiation to the environment were 20 W/m^2-K and 0.3, respectively [27]. The welding structural analysis employed a spring-type boundary condition (BC). Specifically, a spring with a small stiffness of 10 N/mm is attached to each of the eight corners of the workpiece to constrain displacement freedoms in all three Cartesian directions, thereby representing the workpiece loosely set on a flat worktable without any fixturing.

3.2. Austenite-martensite transformations in Grade 91 steel

The G91 base metal microstructure used in this study was a tempered martensite. Complex phase transformations take place during welding. For example, during heating, the tempered martensite can transform into austenite which in turn can transform into delta ferrite if the local temperature is sufficiently high. Due to G91's high hardenability, martensite readily forms from austenite under a typical weld cooling rate. From a residual stress and distortion perspective, the main phase transformations of interest are the martensite (tempered or untempered) transformation to austenite (M-A) during heating, and the reverse austenite transformation into fresh/untempered martensite (A-M) during cooling. This is because these phase transformations induce changes in both material volume and mechanical properties, e.g., yield strength, consequently influencing stress and distortion evolution [28,29]. During multi-pass welding, the martensite formed in a prior pass can be tempered by heat input from subsequent passes. For example, it has been shown that Grade 92 steel, a ferritic-martensitic steel in the same family as Grade 91 steel, can be tempered in the HAZ during gas tungsten arc welding [30]. Additionally, in the model without considering tempering during welding, the residual stress can be slightly overpredicted. Note the martensite in G91 steel has a sluggish tempering kinetics; for example, soaking for 2 h at 1005 K was used to temper the G91 weld in this study, which is much longer compared to the welding thermal cycles [31]. Therefore, the tempering induced during welding is assumed to be negligible. Hence, the microstructure evolution in G91 weld can be described as $f_a + f_m + f_{tm} = 1$, where f_a, f_m, f_{tm}, is the volume fraction of austenite, fresh martensite, and tempered martensite, respectively. The first two are formed during welding, and the last (f_{tm}) comes from the base metal.

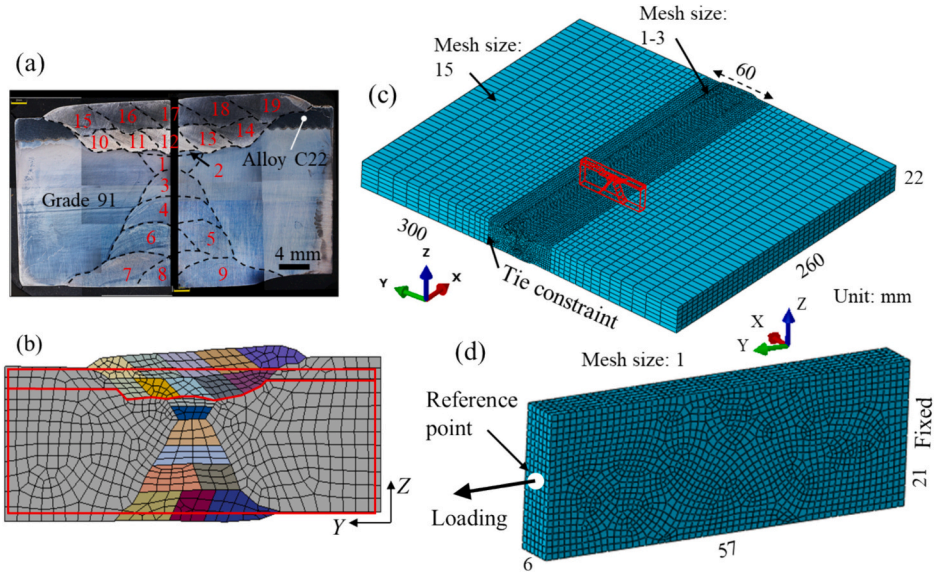

Fig. 2. (a) Weld macrograph on the transverse cross-section, highlighting the fusion lines of individual beads. Welding analysis geometry and mesh (b) on the transverse cross-section, showing the setup of beads, and (c) in 3D view. The coordinate system was set up in such a way that the X, Y, and Z directions are aligned with the length, width and thickness direction of the weldment, respectively. (d) Tensile testing analysis geometry and mesh. The geometry corresponds to a section of the welding analysis geometry, as indicated by red boxes in b and c. (For interpretation of the references to colour in this figure legend, the reader is referred to the web version of this article.)

Fig. 3 shows two typical temperature profiles: one for single-pass and the other for multi-pass welding scenarios. In this single-pass scenario, the temperature profile exhibits a single peak above A_3, and the temperature decreases below the martensite finish temperature (M_f) during cooling. When a G91 steel is subject to this single-pass temperature profile, the M-A and A-M transformations would proceed to completion during heating and cooling, respectively. The transformation kinetics are described by the following equations.

First, the M-A transformation during heating is assumed to be linear with temperature,

$$f_a = \frac{T - A_1}{A_3 - A_1}, (A_1 \le T \le A_3) \quad (1)$$

where $A_1 = 1093$ K and $A_3 = 1193$ K are the austenite transformation start and finish temperatures for G91 steel, respectively [32]. Second, the A-M transformation during cooling is governed by Koistinen-Marburger relationship,

$$f_m = 1.17\{1 - exp[-0.011(M_s - T)]\}, (M_f \le T \le M_s) \quad (2)$$

where T is the temperature, $M_s = 648$ K and $M_f = 473$ K are the martensite start and finish temperatures for G91 steel, respectively [32].

While these complete transformations are readily handled, multi-pass welding causes incomplete transformations when a region does not heat above A_3 or cool down below M_f during a thermal cycle. Particularly, the likeliness of incomplete A-M transformation is greatly heightened when the martensite start temperature is relatively low and the inter-pass temperature is relatively high. For example, the multi-pass temperature profile in Fig. 3 exhibits three cycles, representing preceding (n-1), current (n), and subsequent (n + 1) passes. Incomplete M-A and A-M transformations occur, respectively, at Point P_a (the 1st peak between A_1 and A_3) and Point P_b (the 2nd valley between M_s and M_f). In the literature, discussions on incomplete transformations are relatively limited, and the method used in this study is described as follows.

First, Point P_b in Fig. 3 experiences an incomplete A-M transformation during cooling of Pass n, resulting in formation of some fresh martensite. In Pass n + 1, the fresh martensite is retained as the local peak temperature does not exceed A_3. The mixture of austenite and martensite being reheated can result in complex microstructural changes, such as carbon partitioning (< 10s) from the supersaturated martensite to the untransformed austenite as reported in the literature for quenched and partitioned (Q&P) steels [33]. In such cases, the carbon enrichment in the untransformed austenite raises its chemical stability, and the effective M_s-M_f temperature range is suppressed. For simplicity, this study does not consider the complex microstructural changes. Instead, it assumes that during cooling of Pass n + 1, new martensite does not start to form when the temperature drops below M_s due to the presence of martensite in the microstructure. The threshold temperature for A-M transformation, T_m^{th}, is derived from Eq. (2),

$$T_m^{th} = M_s + ln\left(1 - \frac{f_m}{1.17 f_{max}}\right) \Big/ 0.011, (M_f \le T \le M_s) \quad (3)$$

where f_{max} is calculated by adding the current fractions of austenite and martensite, which also represents the maximum amount of martensite that can be formed at this material point. It is noted that Eq. (3) is also valid when there is only austenite present prior to cooling (e.g., single-pass in Fig. 3). In such a case, $f_m = 0$, and thus $T_m^{th} = M_s$.

The modified fraction of martensite formed in the presence of incomplete A-M transformation can be written by modifying Eq. (2) as,

$$f_m = f_{max} \bullet 1.17\{1 - exp[-0.011(M_s - T)]\}, (M_f \le T \le T_m^{th}) \quad (4)$$

Second, Point P_a in Fig. 3 experiences an incomplete M-A transformation during the heating of Pass n-1. When it is reheated in Pass n, the onset temperature of M-A transformation is altered in the presence of residual austenite. Following a similar approach used previously for the incomplete A-M, the threshold temperature for M-A transformation, T_a^{th} is derived from Eq. (1),

$$T_a^{th} = A_1 + f_a(A_3 - A_1), (A_1 \le T \le A_3) \quad (5)$$

When the temperature is above T_a^{th}, the amount of austenite formed in the microstructure is still calculated by Eq. (1).

With the above equations to track the fractions of austenite and martensite as a function of temperature, the phase transformation induced volume change strain $\Delta\varepsilon_V$ is further calculated by,

$$\Delta\varepsilon_V = V_i \Delta f_i \quad (6)$$

where V is the maximum volume change strain, and the subscript i = a or m represents M-A or A-M transformation, respectively. $V_a = -2.288 \times 10^{-3}$, and $V_m = 3.75 \times 10^{-3}$ [32].

3.3. Post-weld heat treatment model

The PWHT model incorporates creep behavior during the holding stage and plastic redistribution arising from temperature-dependent mechanical properties during both the heating and cooling stages. This approach is justified as the literature studies have shown that creep deformation during heating and cooling is negligible for G91 steel [34,35]. In this study, only the steady-state creep deformation is considered, and it is assumed to obey Norton's law [34],

$$\dot{\varepsilon}_{CR} = A\sigma^n \quad (7)$$

where $\dot{\varepsilon}_{CR}$ is the creep strain rate, σ is the applied stress, and A and n are temperature-dependent material constants. Yaghi et al. [35] determined these two constants for G91 steel by stress relaxation tests at 760 °C: $A = 1.10^{-20}$ and $n = 10.741$ (for stress in MPa). Since the holding temperature applied in this study is close to that used in their study, their measured values were adopted here. Additionally, due to the lack of creep data, C22 is assumed to undergo creep as G91 with the same parameters.

It is noted that tempering of martensite takes place during PWHT of the G91 weld. The change in mechanical properties of FZ and HAZ due to tempering (e.g., through carbide precipitation) [36], is not considered for simplicity. The literature has shown that the predicted residual stress aligns well with experimental data in the absence of tempering considerations [28,35,37].

Due to the slow heating and cooling rates and relatively thin section of the welded plate, the entire plate temperature was assumed to follow that used in PWHT. The PWHT analysis employed the same BC as the

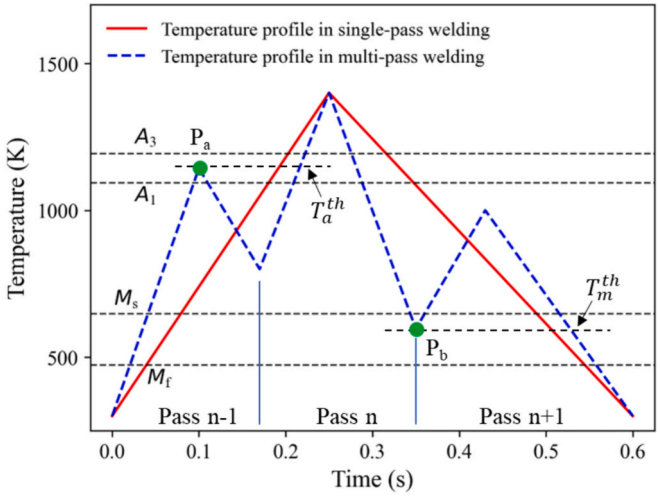

Fig. 3. Schematic temperature profiles for complete and incomplete transformations in single- and multi-pass welding, respectively.

structural analysis in Section 3.1.

3.4. Material thermomechanical properties

The welding analysis employs a thermo-elasto-plasticity constitutive relation, and the PWHT analysis employs a thermo-elasto-visco-plasticity constitutive relation. In the analysis, the total strain increment is decomposed into increments of thermal, elastic, plastic, and creep strains (in the case of PWHT). The thermal strain is calculated as the product of the coefficient of thermal expansion (CTE) and temperature variation, the elastic strain follows Hook's law of linear elasticity, the plastic strain adheres to the flow rule with a von Mises yielding function and an isotropic hardening formulation, and the creep strain is calculated using Eq. (7).

Fig. 4a shows the thermal and mechanical properties of G91 utilized in welding and PWHT analysis, including thermal conductivity λ, specific heat C_p, CTE, elastic modulus E, yield strength of base metal σ^b_{yield} and weld metal σ^w_{yield}. Additional properties used in the analysis but not shown in the figure include density ($\rho_{G91} = 7770$ kg/m^3), fusion latent heat ($H_{G91} = 2.56 \times 10^5$ J/kg•K), solidus temperature ($T_{s\text{-}G91} = 1693$ K), and liquidus temperature ($T_{l\text{-}G91} = 1773$ K). Part of these properties are sourced from the work by Kiranmayi [38]. The values of σ^b_{yield} and σ^w_{yield} are adopted from experimental measurements by Deng et al. [28]. Plastic hardening is omitted due to the relatively low strain values incurred during welding (e.g., < 20 % [39,40]). Due to incomplete M-A and A-M transformations described in Section 3.2, the yield strength of a mixture of martensite and austenite phases, σ^{mix}_{yield} is estimated using,

$$\sigma^{mix}_{yield} = f_m \sigma^m_{yield} + (1 - f_m)\sigma^a_{yield} \tag{8}$$

where σ^m_{yield} and σ^a_{yield} are the yield strength of fresh martensite and austenite, respectively. Note that σ^m_{yield} is assumed to be equal to that of the weld metal, and σ^a_{yield} is assumed to follow the temperature-dependent yield strength of the base metal σ^b_{yield} (see Fig. 4a).

Fig. 4b-c show the thermal and mechanical properties of C22. Given the high work-hardenability of C22, linear hardening as a function of temperature is considered in both the welding and PWHT analyses. Supplementary properties not presented in the figure include $\rho_{C22} = 8690$ kg/m^3, $H_{C22} = 2.56 \times 10^5$ J/kg•K, $T_{s\text{-}C22} = 1630$ K, and $T_{l\text{-}C22} = 1672$ K. All these properties are sourced from the Haynes International online database [41]. As noted previously, dilution in the substrate and clad beads is not considered. In other words, beads 1–9 (see Fig. 2a) are assigned with properties of G91, and beads 10–19 with properties of C22.

3.5. Tensile testing model

Fig. 2d shows the geometry of tensile testing analysis with dimensions of 57 mm long × 6 mm wide × 21 mm thick, which represents the gauge section of the experimental tensile specimen. This geometry is extracted from a section of the welding analysis geometry, as indicated by red boxes in Fig. 2b-c. The initial condition of the tensile sample is established based on the final state of the welding and PWHT analysis, utilizing data mapping from the old mesh to the new mesh. This data mapping is executed through a two-step interpolation technique [42]. In the first step, the data is acquired at the nodes of the old mesh by extrapolating from integration points to the nodes of each element. Subsequently, the integration points of the new mesh are mapped to the old mesh, and the values at these integration points are obtained by interpolating from the nodes of the old mesh. As shown in Fig. 2d, a uniform mesh with a size of 1 mm was employed to ensure accurate data transfer.

The tensile testing analysis consisted of two steps. Step 1 addressed the stress unbalance due to the extraction from the weldment. Note that the mechanical properties used in the tensile testing analysis were derived from experimental measurements of post-weld heat treated sample, which had already undergone removal of prior work hardening effects. Hence, the equivalent plastic strain, which induces work hardening, was removed via "annealing" in this step. Step 2 simulated the experimental tensile testing by fixing the right face and loading on the left surface, as shown in Fig. 2d. The left face was coupled to a reference point using the kinematic coupling constraint, and a displacement in the

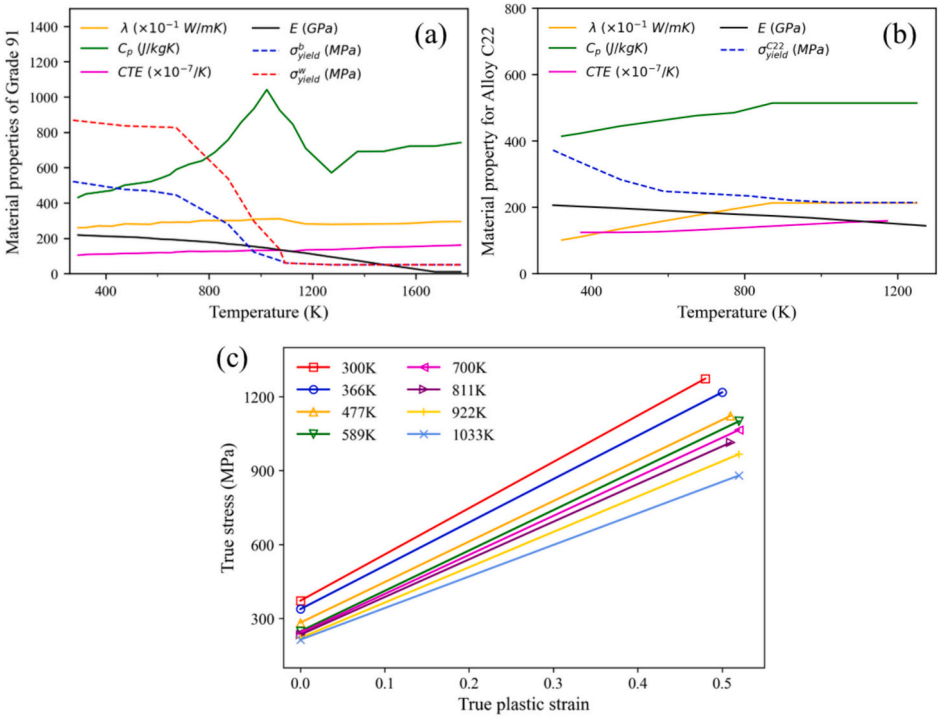

Fig. 4. Thermophysical and mechanical properties of (a) G91 and (b) C22. (c) Temperature-dependent stress-strain relations of C22.

loading direction was assigned to the reference point with displacement freedoms in all other directions fixed. To show the effect of residual stress, a comparative simulation case was also conducted by omitting the incorporation of the stress (i.e., without Step 1) while keeping everything else the same.

The tensile testing analysis employs an elasto-plasticity constitutive relation. The microstructure of the G91 weld is highly inhomogeneous, and microstructure-dependent stress-strain curves are thus essential to accurately simulating the tensile testing. However, due to experimental limitations, the individual stress-strain curves for different microstructure regions such as G91 weld metal were not measured. The following simplifications are used to obtain the necessary mechanical properties.

First, from the tensile test of a cross-weld sample at room temperature (Fig. 2d), a stress-strain curve was obtained following the procedure shown in Appendix A. This stress-strain curve was then assigned to the G91 base metal and HAZ. This simplification is justified as the deformation primarily occurred in the G91 base metal (to be shown later). Additionally, the measured ultimate tensile stress (UTS) of the cross-weld sample was 675 MPa (Fig. A.1), which is comparable to the typical UTS value of 683 MPa for G91 base metal [43].

Second, as to be shown later (Fig. 9e), the hardness value of the G91 base metal and HAZ was relatively uniform even though there were several soft spots corresponding to inter-critical HAZ. Specifically, the soft spots had a hardness of 200 HV and the rest of the HAZ 220 HV. Given the relatively small difference in hardness, the soft spots were assumed to have the same stress-strain curve as the base metal and HAZ determined above.

Third, the G91 weld metal has a much higher hardness than the base metal (see Fig. 9e to be discussed later). The stress-strain curve for the G91 weld metal was determined by multiplying the base metal flow stresses by the hardness ratio, 260 HV for weld metal / 220 HV for base metal. Additional details can be found in Appendix A.

Lastly, the C22 base metal and weld metal are assumed to follow the mechanical property at room temperature shown in Fig. 4c.

3.6. Model implementations

The integrated process-performance modeling was executed using Abaqus [42], a commercial finite element solver. The weld structural and tensile testing analyses were handled by a STATIC step, while the PWHT was handled by a VISCO step, which is used to account for time-dependent creep behavior in a quasi-static analysis [42]. The element type used in the thermal and mechanical analysis is full-integration brick element.

For ease of implementation, the volume change strain due to M-A and A-M transformations is added to the thermal strain in the calculation. Specifically, two Abaqus user subroutines were used: USDFLD which tracks the microstructure evolution as a function of temperature, and UEXPAN which calculates the volumetric strain due to phase transformations. A verification case for the incomplete transformations along with the Fortran source codes are provided in Supplemental Sections 1 and 2, respectively.

The welding thermal and mechanical analyses required 11 h and 36 h, respectively, utilizing a workstation equipped with a 16-core AMD 1950X processor and 32 GB of RAM. The total element count for each analysis amounted to 93,674. The tensile testing analysis cost 20 min on the same machine with a total element count of 28,160.

4. Results and discussion

4.1. Temperature and stress fields during welding and PWHT

Fig. 5a shows a representative temperature field during welding; it is for pass 9, the final substrate pass, at an instance when the welding torch passes the mid-length plane. Due to the concentrated arc energy input, a steep temperature gradient is present around the molten pool. Such

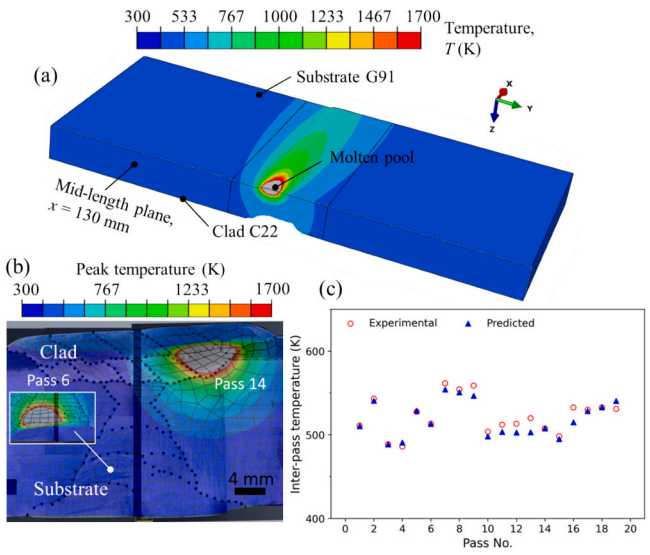

Fig. 5. (a) Representative temperature field and molten pool for pass 9 when the welding torch passes the mid-length plane. Verification for welding thermal analysis using (b) fusion boundary and (c) inter-pass temperatures of individual passes.

temperature gradient is a main driving force for the formation of residual stress and distortion [44]. Fig. 5b shows the peak temperature distribution on a cross-section for pass 14, with the boundary of the predicted fusion zone depicted by the liquidus temperature contour (e.g., $T_{\text{l-C22}}$ for this pass). When compared to the experimentally measured fusion boundary depicted by dotted lines, a good consistence is observed. Similarly, the inset image shows a good consistence between the experimental and predicted fusion boundary for pass 6. Additionally, Fig. 5c shows the predicted inter-pass temperatures are consistent with the experimental data of individual beads. Such consistence is expected as the Goldak heat flux parameters were calibrated against the fusion boundaries in the thermal analysis. Nevertheless, the consistence provides some basis to support the validity of the calculated temperature field for stress and distortion analysis.

As an example of stress evolution, Fig. 6a shows the distribution of transverse stress (σ_Y) at the end of the cooling phase of pass 9. Some tensile stress forms in the region beneath the cap passes on the substrate side, as marked by a dashed ellipse. In particular, σ_Y reaches the peak just beneath the freshly deposited bead of pass 9. Fig. 6b shows the σ_Y distribution at the end of welding, i.e., after the entire weldment is cooled down to room temperature. The tensile stress is also observed beneath the cap passes on the clad side. Additionally, the tensile stress on the substrate side is significantly increased when compared to that prior to welding of the clad layer (Fig. 6a).

Fig. 7 compares the stress distribution on the transverse cross-section in the as-welded versus after PWHT state. Fig. 7a-b show the as-welded stress in the longitudinal (σ_X) and transverse (σ_Y) directions, respectively. σ_X is predominantly tensile in the FZ and HAZ and transitions to compressive stress in the base metal. In contrast, σ_Y exhibits a tensile-compressive-tensile pattern along the thickness direction in the FZ, accompanied by marginal stress in the base metal. Overall, it is concluded that the high tensile stress is concentrated in the weld metal, particularly in the cap passes on both sides, whereas stress in the base metal remains low and compressive.

Fig. 7c-d show σ_X and σ_Y after PWHT. In the FZ of the substrate, both σ_X and σ_Y exhibit notable reductions with peak tensile stress decreased to only about 100 MPa (yellow contours around the substrate's cap passes). In the FZ of the clad, both σ_X and σ_Y also exhibit some reductions although the peak tensile stress is higher than that in the FZ of the substrate. Specifically, σ_X ranges from 150 to 270 MPa (orange and red contours) and σ_Y ranges from 100 to 200 MPa (yellow and orange

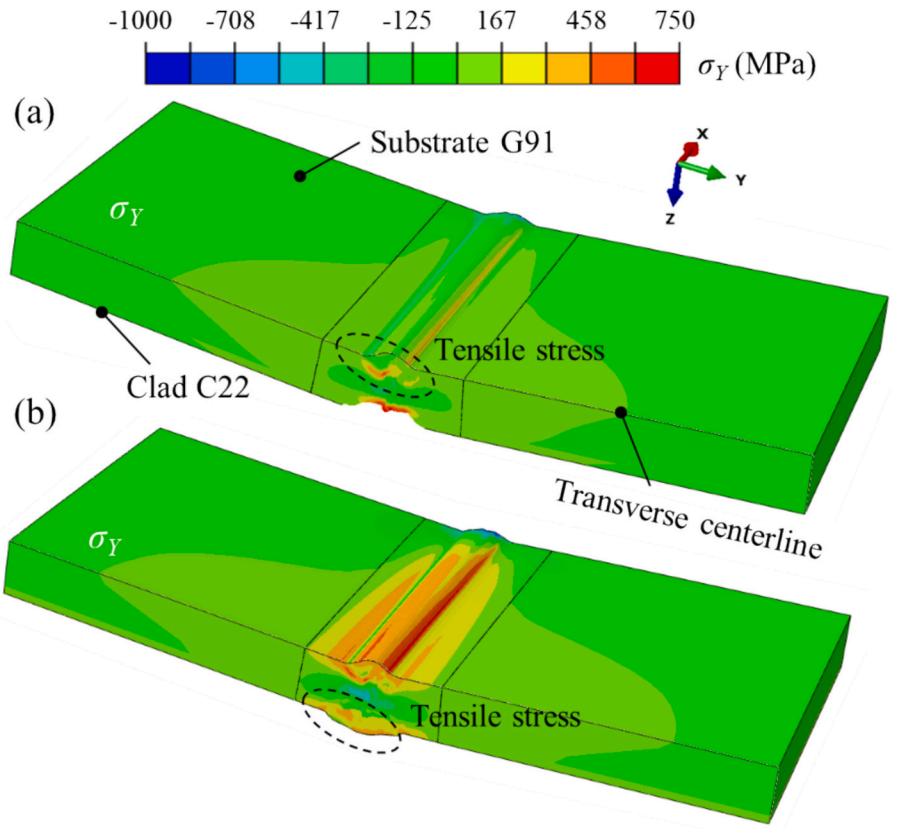

Fig. 6. Distribution of transverse stress (σ_Y) at the end of (a) cooling phase of pass 9, and (b) welding, i.e., after the entire weldment is cooled down to room temperature.

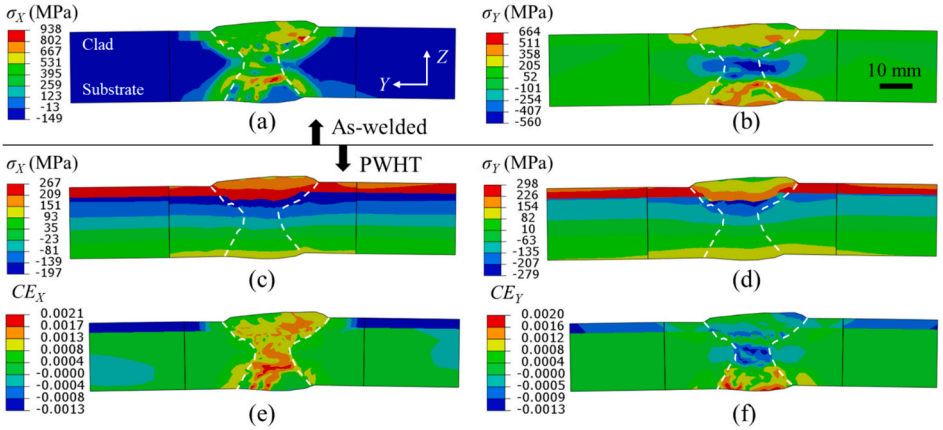

Fig. 7. As-welded stresses in the (a) *X* direction and (b) *Y* direction, stresses after PWHT in the (c) *X* direction and (d) *Y* direction, and creep strains after PWHT in the (e) *X* direction and (f) *Y* direction. The transverse cross-section is located at the center of the weld plate along the length direction.

contours). Unlike the FZ, the base metal of the clad experiences an increase in residual stress after PWHT, with high tensile σ_X and σ_Y reaching peak values of about 250 MPa. Furthermore, a high stress gradient is present at the bonding interface, marked by a transition from high tensile stress to high compressive stress, particularly in the case of σ_X.

The elevated tensile stress in the clad and the high stress gradient at the bonding interface after PWHT are attributed to the mismatch in CTE between the clad and the substrate. Specifically, the average CTE of the clad material is 11.6 % larger than that of the substrate within the temperature range of 300–1005 K (see Fig. 4). The excess thermal expansion of the clad material is constrained by the substrate during the heating phase of PWHT, and the resulting compressive plastic strain leads to tensile stress in the clad after PWHT [14]. Fig. 7e-f show the creep strain after PWHT in the longitudinal (CE_X) and transverse (CE_Y) directions. The patterns of creep strains align with the respective stresses, which is expected as the magnitude of creep strain is proportional to the magnitude of stress (Eq. (7)).

In summary, PWHT has dual effects on the residual stress in the G91/C22 weld. On one hand, it mitigates residual stresses in the weld metal through creep deformation. On the other hand, the mismatch in CTE between the clad and the substrate induces tensile stress in the clad layer and a high stress gradient at the bonding interface. Those results are consistent with observations reported in the literature [14,15,45].

Due to experiment limitations, the residual stress was not measured.

Instead, the displacement of the plate in the Z direction (U_Z) was experimentally mapped and used to validate the mechanical analysis for welding and PWHT. Fig. 8a depicts the experimentally measured U_Z when the substrate side is facing upwards. Note that due to limitations in the measurement apparatus, the middle section (-70 mm $< y <$ 70 mm) was not measured. Overall, two bending distortion patterns are observed. Pattern 1 is bending about the Y direction, indicated by the increase in magnitude of U_Z as one moves along the longitudinal direction from $x = 500$ to 0 mm. Pattern 2 is bending about the X direction, indicated by the increase in magnitude of U_Z as one moves from the center towards the outer side along the Y direction. It is noted that Pattern 2 is commonly observed in butt-welded plates but Pattern 1 is unexpected. Fig. 8b shows the calculated displacement field in the Z direction after PWHT, showing the predominant "butterfly"-shaped

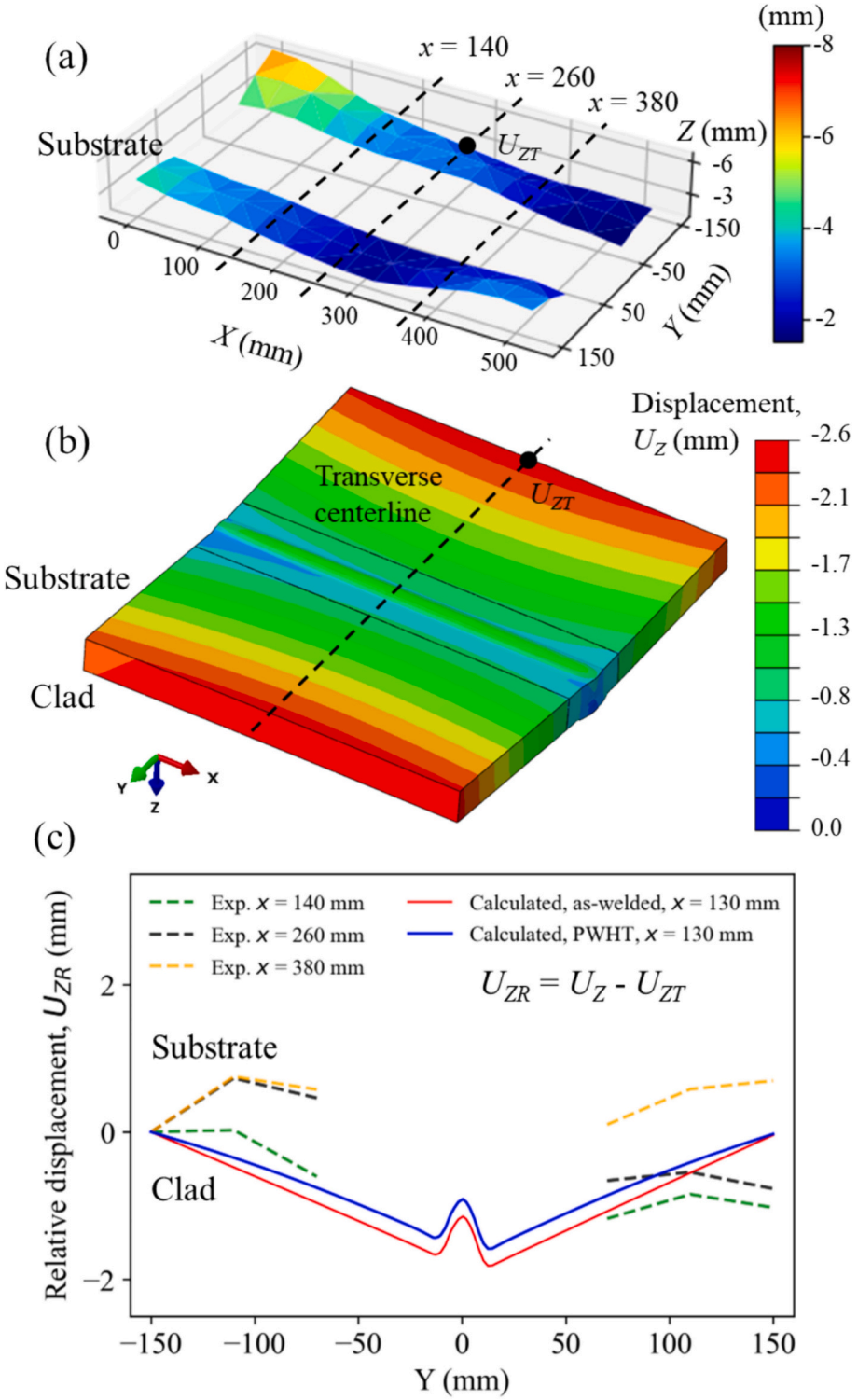

Fig. 8. Validation of welding and PWHT mechanical analyses through distortion assessment. (a) Experimentally measured displacement in the Z direction when the substrate side is facing upwards. (b) Calculated displacement field in the Z direction after PWHT. (c) Comparison of the Z displacement profiles in the transverse direction between experimental and calculated results.

distortion about the X direction. This bending, commonly observed in a butt weld, is attributed to the unbalanced shrinkage force between the substrate and the clad [44].

For a more quantitative comparison of the predicted and measured distortion, the line profile of U_Z along the Y (or weld width) direction is compared as shown in Fig. 8c. For the measured distortion, three locations near the plate's mid-plane were selected: x = 140, 260, and 380 mm, as shown in Fig. 8a. For the simulation data, only the mid-plane was selected since the bending distortion is relatively uniform along the X direction. The extracted data was then used to define a relative Z displacement, $U_{ZR} = U_Z - U_{ZT}$, where U_{ZT} is the Z displacement at the midpoint of the top edge, as indicated in Fig. 8a-b. This conversion is needed partly due to the inconsistent reference for measurement between experiment and simulation, coupled with the unexpected bending pattern 1 in the experiment.

As shown in Fig. 8c, the three experimental U_Z profiles demonstrate the two bending patterns. Furthermore, both the experimental (dashed lines) and calculated (solid blue line) data display bending pattern 2, although the magnitude of the bending is not accurately calculated. In summary, the comparison shows bending pattern 2 was predicted by the model but pattern 1 was not. A possible reason is the experimental error; for example, Fig. 2a shows there were some misalignments between the two plates during welding. Lastly, superimposed in Fig. 8c is the as-welded distortion (solid red line) which is close to the distortion after PWHT, suggesting that the PWHT has a limited effect on reducing distortion.

Although the predicted stress and distortion are not fully validated due to the experimental limitations, the final residual stress distribution, dominated by PWHT, is deemed sufficient for subsequent tensile modeling in conjunction with the weld microstructure to be described next.

4.2. Phase fractions after welding

As noted previously, the microstructure in the G91 substrate weld is described by austenite, fresh martensite, and tempered martensite with the following relation $f_a + f_m + f_{tm} = 1$. As an example of the predicted microstructure evolution, Fig. 9a-b show the calculated distribution of fresh martensite and austenite, respectively, at the end of the cooling phase of pass 8. Note that the microstructure of base metal comprises solely tempered martensite, thus exhibiting 0 value on each plot. The incomplete A-M transformation, exacerbated by a high inter-pass temperature of ~552 K (Fig. 9c), results in a mixed microstructure of fresh martensite and remaining austenite. The retained austenite in pass 8 is eventually transformed into martensite after the weldment is cooled down to room temperature. Consequently, the FZ is completely transformed to fresh martensite in the final state, as shown in Fig. 9d. This incomplete A-M transformation alters the local volume strain and mechanical properties, and the evolution of stress and distortion considering these effects is already presented in the previous section.

Fig. 9d also shows patches in the HAZ that contain a mixed microstructure of tempered and untempered martensite. These patches, belonging to the inter-critical HAZ, experienced incomplete M-A transformations (see Eq. (1)), thus retaining some of the tempered martensite from the base metal. The predicted IC-HAZ is predominantly observed at the waist of the FZ and beneath the cap passes, as marked in Fig. 9d. These locations experienced multiple thermal cycles in such a way that the local IC-HAZ was significantly widened. As reported in the literature, the IC-HAZ exhibits lower hardness than both the base metal and the fine-grain HAZ after PWHT [46]. In the experimentally measured hardness map (Fig. 9e), soft spots are observed at locations aligning with the predicted IC-HAZ patches. Such consistency supports the validity of the weld thermal analysis and the metallurgical analysis considering incomplete transformations. It is noted that the IC-HAZ, typically with a width of 0.2–0.4 mm [47,48], cannot be fully captured by the present model with a mesh size of 0.5–1.5 mm across the HAZ. Similarly, the experimental hardness map did not fully capture the IC-HAZ due to the large indent spacing used (e.g., 0.5 mm along the weld width direction).

4.3. Tensile testing analysis

Fig. 10a-b shows the experimental DIC strain maps during tensile testing of the cross-weld sample at engineering strain (ε_{YE}) levels of approximately 3 % and 15 %, respectively. In the early stage of loading (ε_{YE} = 3 %), the deformation is primarily distributed in the G91 base metal (near the weld) and the C22 weld metal as marked in Fig. 10a (purple-colored contour). Conversely, the G91 weld metal exhibits negligible deformation. At the point of fracture (ε_{YE} = 15 %), a high deformation zone, is observed in a lower region in the G91 base metal, highlighting localized necking inclined in the loading direction. The final fracture occurs along the direction of the localized necking, as indicated in the bottom-right inset of Fig. 10c. Note that the base metal further away from the weld does not deform significantly, primarily due to fixturing.

From the DIC strain map, local Y-strain (ε_Y) histories at three monitoring points – C0, C1 and C2– were extracted, as shown in Fig. 10b. Points C1 and C2 were positioned along a vertical line, which passed through the high deformation zone, with the former placed approximately at the plate's mid-thickness and the latter in the clad layer. Point C0 was located 5 mm horizontally from C1 towards the G91

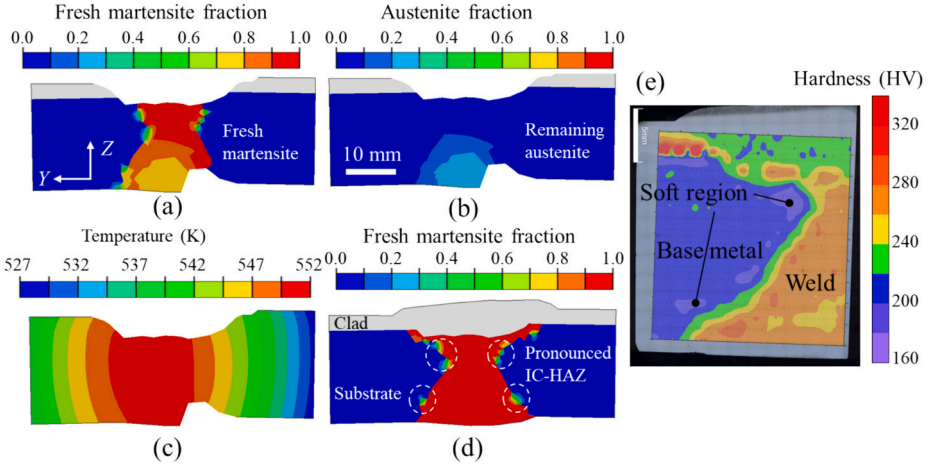

Fig. 9. Calculated distribution of (a) fresh martensite, (b) austenite, and (c) temperature at the end of the cooling phase of pass 8. (d) Calculated distribution of fresh martensite at the end of welding. (e) Experimentally measured hardness map of weld and adjacent heat-affected zones after PWHT.

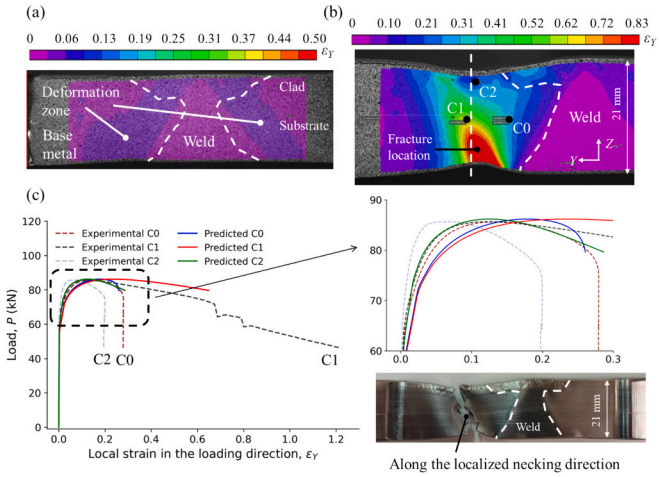

Fig. 10. DIC strain map for RT experimental tensile test at engineering strain levels of approximately (a) 3 % and (b) 15 %, respectively. (c) Load-strain curves comparison of experiment to simulation at three monitoring points, C0, C1 and C2. Points C1 and C2 are approximately located at the mid-thickness and in the clad layer, respectively, along a vertical line through the high deformation zone, while point C0 is located 5 mm horizontally from C1 towards the G91 weld metal. (For interpretation of the references to colour in this figure legend, the reader is referred to the web version of this article.)

weld metal. In accordance with the experiment, the calculated strain histories at the same monitoring locations were extracted from the tensile model (see Fig. 11d), and the reaction force at the reference point (see Fig. 2d) was also extracted as the calculated load.

Fig. 10c compares the experimental versus calculated load versus local *Y*-strain curves (L-ε_Y) for the three monitoring locations. Specifically, all the experimental curves exhibited a rapid linear increase in load initially that was followed by a gradual rise until the peak load was reached at a local strain of 5 % to 10 %. Afterward, the necking was able to reduce the cross-section area to such a sufficient level that the load needed to further deform the sample started to drop. As the further deformation was concentrated in the necking region (Fig. 10b), C1, located near that region, experienced high strain prior to the final failure. On the other hand, C2 and C0, located away from the necking region, did not experience much additional deformation, resulting in a steep drop in load prior to failure, as shown in Fig. 10c.

The deformation behavior of C0 and C1, both in G91 with the former away from the necking region and the latter near it, is well captured by the tensile model, as shown in Fig. 10c and a zoom-in view in the top-right inset of Fig. 10c. Some discrepancy is noted; for example, the model underpredicted the local strain and slightly overpredicted the load at point C1 towards the late portion of loading when the local strain was above 30 %. Such deviation is attributed to the final fracture, which is not accounted for in this model. At point C2, the load was overpredicted when the local strain was above 10 % (e.g., prediction 83 MPa vs. experimental 74 MPa at a strain of 20 %). This deviation is likely attributed to inaccuracies in the mechanical properties of C22 as well as a lack of consideration of the final fracture. Overall, the comparison in Fig. 10c shows some fair agreements between experimental and calculated load-strain curves at the three different locations, validating the tensile testing analysis.

Fig. 11a-d show the calculated distribution of strain in the loading direction (ε_Y) during the tensile test at four different engineering strain (ε_{YE}) levels of 3 %, 6.8 %, 12 % and 15 %, respectively (see Appendix Fig. A.1). Specifically, Fig. 11a depicts that at the early stage of loading, deformation zones are observed on both sides of the weld metal, with pronounced deformations in the G91 base metal and the C22 weld metal, and minimal deformations in the G91 weld metal. This predicted deformation pattern is consistent with the experimental strain map shown in Fig. 10a. When necking started to take place (Fig. 11b), the high deformation zone is confined solely to the G91 base metal, whereas the deformation is relatively uniform in the clad. In the post-necking stage (Fig. 11c-d), the G91 base metal undergoes additional deformation, resulting in a high deformation zone inclined to the loading direction. This high deformation zone aligns with the experimentally observed localized necking in Fig. 10b.

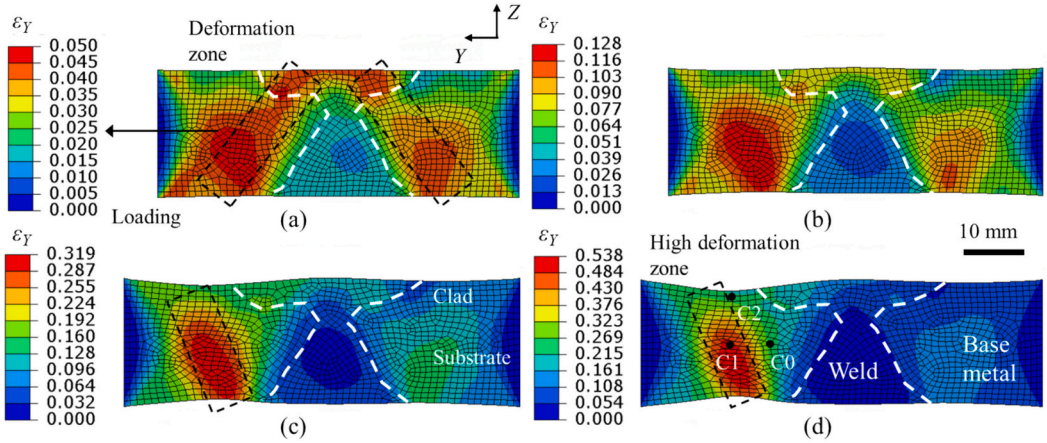

Fig. 11. Predicted distribution of strain in the loading direction at engineering strain levels of (a) 3 %, (b) 6.8 %, (c) 12 %, and (d) 15 %, respectively (see Appendix Fig. A.1).

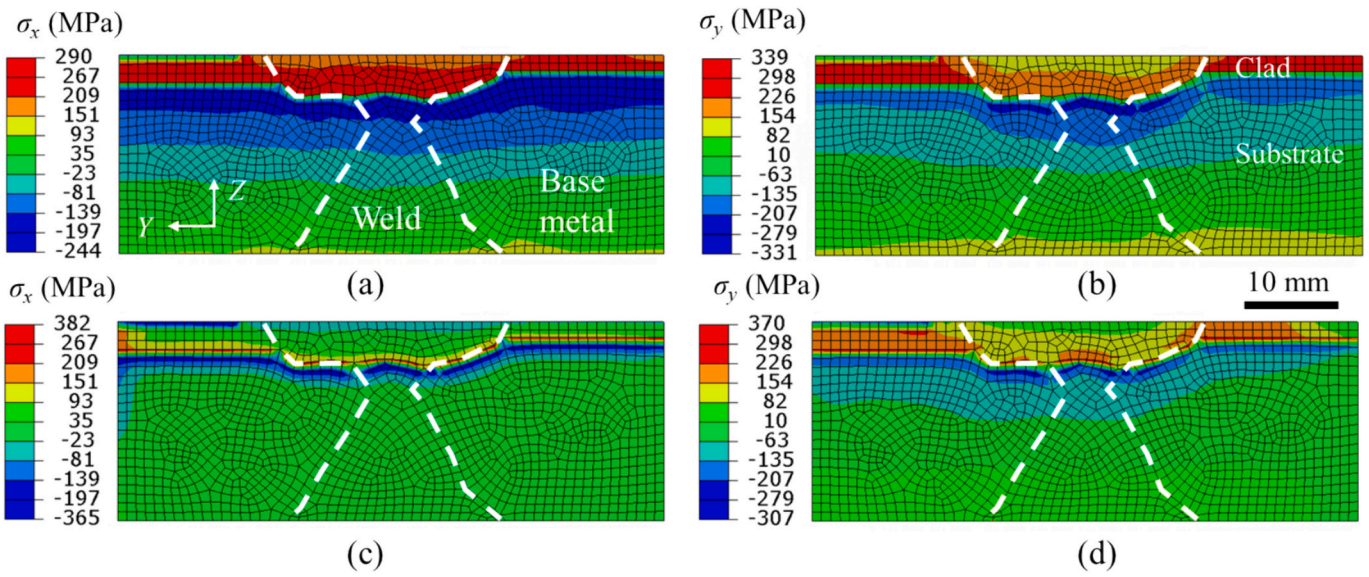

Fig. 12. Calculated distribution of stress in the tensile specimen prior to tensile loading: (a) σ_X and (b) σ_Y as-mapped from the welding and PWHT analysis. (c) Redistributed σ_X and (d) σ_Y after the re-balance step representing mechanical sectioning.

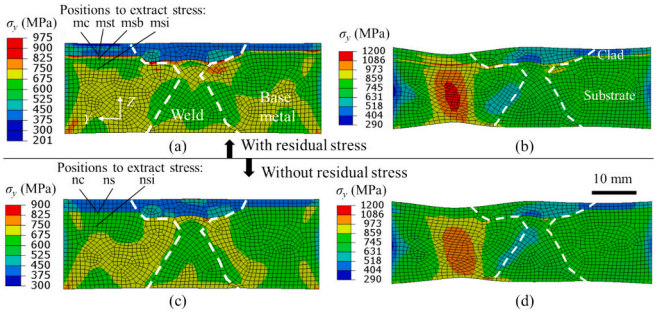

Fig. 13. Calculated distribution of stress during tensile loading. σ_Y at engineering strain levels of (a) (c) 3 % and (b) (d) 15 %. (a)(b) correspond to the case incorporating residual stress from welding and PWHT, while (c) (d) correspond to the case without considering residual stress. Positions such as mc and nc marked in (a) and (c) were used to extract characteristic stresses with detailed results presented in Appendix B.

Fig. 12 shows the calculated distribution of stress in the tensile specimen prior to tensile loading. The initial stress distribution in the specimen was mapped from the welding and PWHT analysis. Fig. 12a-b show the as-mapped σ_X and σ_Y, respectively, which closely align with the respective source results in Fig. 7c-d, respectively. As noted in Section 3.5, the first step of the tensile testing analysis was to re-balance the stress, representing stress relieving due to mechanical sectioning. The effect of stress relieving is observed in Fig. 12c-d, where σ_X and σ_Y experienced redistribution. Specifically, σ_X was largely reduced as the cross-weld sample had a much smaller dimension along the weld length direction compared to the full geometry. On the other hand, σ_Y exhibited a moderate reduction of ~50 MPa as the sample maintained a large fraction of the weld width dimension. Lastly, the strong stress gradient at the bonding interface, with tensile stress in the clad and compressive stress in the substate, was also retained.

Fig. 13 shows the calculated distribution of stress during tensile loading. At the early stage of tensile loading ($\varepsilon_{YE} = 3$ %), Fig. 13a shows that σ_Y in the clad approximately equals the yielding stress of C22, indicating a small level of plastic hardening. In contrast, the G91 base metal undergoes a considerable amount of plastic hardening, resulting in σ_Y significantly surpassing its yield stress of 464 MPa. A reason for the disparity in the stress between the clad and substrate is provided in the following. In tensile testing, the clad and the substrate maintain the same length versus load as the two are bonded together. For the substrate, the G91 weld metal exhibits a higher hardness and thus a higher strength than the G91 base metal ($\sigma^b_{yield} = 464$ MPa, and $\sigma^w_{yield} = 548$ MPa as shown in Appendix Fig. A.1b). Since the two regions are connected "in series" along the loading direction, the stretched length increase is largely absorbed by the softer base metal, resulting in a larger plastic hardening in the G91 base metal. On the other hand, the C22 weld metal and its base metal have comparable strength. As a result, the C22 weld

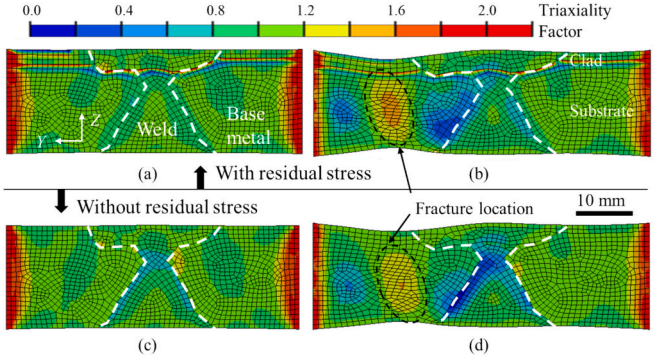

Fig. 14. Stress triaxiality factor at engineering strain levels of (a) (c) 3 % and (b) (d) 15 %. (a)(b) correspond to the case incorporating residual stress from welding and PWHT, while (c) (d) correspond to the case without considering residual stress.

metal and base metal are stretched more uniformly, and as a result no extensive plastic hardening occurs in the clad.

As noted earlier, necking reduces the cross-sectional area to carry the load, exacerbating the increase in the local stress. At the fracture point (ε_{YE} = 15 %), the G91 base metal, accumulating substantial plastic hardening, exhibits the highest σ_Y, as shown in Fig. 13b. The stress pattern aligns with the localized necking in Fig. 10b and high deformation zone in Fig. 11d.

As noted in Section 3.5, a comparative tensile testing case was run where the tensile sample was initially stress-free without any residual stress from welding and PWHT. Fig. 13c-d show σ_Y at ε_{YE} = 3 % and 15 %, respectively for this comparative case. Similar σ_Y patterns are observed between the two cases, except that the high tensile stress at the bonding interface was not captured when the residual stress was not included. This high tensile stress is attributed to the interaction between the residual stress and the tensile loading stress. As the sample underwent tensile loading, the initial compressive stress in the substrate gradually diminished and shifted to tensile stress, while the initial tensile stress in the clad was further compounded with the tensile loading stress.

To help understand the fracture mode and location, the triaxiality factor (TF) is computed based on the numerical results. TF is defined as TF = $(\sigma_1 + \sigma_2 + \sigma_3) / \sigma_v$, where σ_1, σ_2 and σ_3 are the maximum, intermediate and minimum principal stresses, respectively, and σ_v denotes the von Mises stress [49]. Fig. 14a-b show the calculated TF at 3 % and 15 % ε_{YE}, respectively for the case incorporating the residual stress. At the early stage of uniaxial tensile loading (ε_{YE} = 3 %), TF distribution exhibits a relatively uniform value of 1.0 except for two locations, i.e., bonding interface and sample's left and right end surfaces. The former is attributed to the high stress gradient at the interface (as detailed in Appendix B), and the latter attributed to the boundary conditions applied at the ends. At ε_{YE} = 15 %, TF reaches a peak at the location aligned with the high deformation zone in Fig. 11d and the high stress zone in Fig. 12f, indicating the fracture initiation in this location. Moreover, the peak TF value of 1.48 suggests a ductile fracture mode [50], consistent with the experimental observation.

The results for the comparative case without residual stress are shown in Fig. 14c-d. Predicted TF values and patterns are again similar between the two cases, except that the comparative case does not capture the high TF value at the bonding interface.

The comparison of the two tensile simulation cases, with and without residual stress from welding and PWHT, indicates that the residual stress plays an insignificant role in the tension fracture behavior of the weld of G91/C22 clad pates. This is because the fracture stress in the G91 base metal is dominated by that from the tensile loading. However, the residual tensile stress can be compounded with the applied load, resulting in significant tensile stress and TF at the bonding interface where a high stress gradient persists. A reason that the interface debonding did not occur in the present study is likely the high bonding strength of the clad to the substrate by explosive welding [51,52]. But it indicates that the residual stress could become a critical factor for cases where the substrate/clad bonding strength is weak.

5. Summary and conclusions

An integrated model, encompassing welding, PWHT and tensile testing, has been developed to study the fracture behavior of a welded bimetallic plate with G91 steel substrate and C22 alloy clad loaded in tension. The simulation results of fusion zone shapes, soft regions in heat-affected zone, and local strains during tensile testing are consistent with the respective experimental data. On the other hand, the predicted distortion does not match that measured experimentally possibly due to some experimental error. The following conclusions can be drawn.

(1) For the multi-pass weld with relatively high inter-pass temperatures, the incomplete austenite-martensite transformations are observed. By considering the incomplete transformation kinetics in the welding model, the IC-HAZ, characterized by a mixed microstructure of tempered and untempered martensite, is predicted. This is particularly evident in areas experiencing more thermal cycles, e.g., locations beneath the cap passes on both sides of the clad plates. The predicted locations of IC-HAZ correlate well with the low hardness spots observed experimentally on a weld transverse section.
(2) Welding introduces tensile stress in the weld metal which is most significant in the vicinity of the cap beads on both the substrate and clad sides. PWHT effectively mitigates the residual stress in the weld metal through creep deformation. However, the larger CTE of the clad material compared to the substrate induces considerable tensile stress in the clad and a high stress gradient at the bonding interface.
(3) During tensile testing, the G91 base metal, weaker than the G91 weld metal, experiences higher deformation. In contrast, the deformation in both the base and weld metals of clad C22 is relatively uniform due to their comparable strength. As deformation accumulates in the G91 base metal, the stress triaxiality there also increases, ultimately leading to fracture. Therefore, the fracture location of the G91/C22 weld is determined by the relative strength between the base and weld metals, rather than that between the clad and substrate materials.
(4) For the G91/C22 weld, the residual stress induced by welding and PWHT has an insignificant effect on the fracture in G91 base metal. However, the residual tensile stress is compounded with the tensile loading stress, especially at the bonding interface where a high stress gradient persists, thereby exacerbating the tensile stress and triaxiality factor in that region. Hence, for cases with a weak clad-substrate bonding strength, the residual stress could be a critical factor in influencing the fracture behavior.

CRediT authorship contribution statement

Xuesong Gao: Writing – review & editing, Writing – original draft, Visualization, Validation, Software, Methodology, Investigation, Formal analysis, Data curation, Conceptualization. **Abdelrahman Abdelmotagaly:** Writing – review & editing, Visualization, Validation, Methodology, Investigation, Formal analysis, Data curation. **Timothy Pickle:** Writing – review & editing, Visualization, Validation, Methodology, Investigation, Formal analysis, Data curation. **Aric Adamson:** Writing – review & editing, Visualization, Investigation, Formal analysis, Data curation. **Chad Augustine:** Writing – review & editing, Supervision, Project administration, Funding acquisition. **Zhenzhen Yu:** Writing – review & editing, Supervision, Software, Resources, Methodology, Funding acquisition, Conceptualization. **Wei Zhang:** Writing – review & editing, Supervision, Software, Resources, Methodology, Funding acquisition, Conceptualization.

Declaration of competing interest

The authors declare that they have no known competing financial interests or personal relationships that could have appeared to influence the work reported in this paper.

Acknowledgements

This research was supported by the Solar Energy Technologies Office (SETO) within the Department of Energy (DOE) and the National Renewable Energy Laboratory (NREL) with Award No. DE-EE00036334. The authors acknowledge Steve Mabry from NobelClad and Benjamin Sprengard from Enerfab for preparing the experimental materials.

Appendix A

Cross-weld samples, extracted from the PWHT'ed. G91/C22 weld joint, were subjected to uniaxial tensile testing at room temperature, as depicted in Fig. 1c. The resulting engineering stress-strain curves for three duplicate samples are presented in Fig. A.1a. The three curves are consistent until the engineering strain exceeds 6.8 %. The data of Sample 2, locating between those of Samples 1 and 3, is used for the present analysis. The yield strength is found to be 464 MPa, and the ultimate tensile strength 675 MPa with a corresponding necking strain of 6.8 %.

The engineering stress-strain curve for Sample 2 is converted into the true stress-strain curve shown in Fig. A1b. Note that the post-necking portion is excluded due to the stress condition deviated from the uniaxial state. Instead, the post-necking behavior is extrapolated from a Hollomon type fitting to the pre-necking portion, as indicated in the figure.

Given that the deformation predominantly occurs in the G91 base metal, the stress-strain relation of the cross-weld sample is assumed to represent that of the G91 base metal. The true stress-strain relationship for the G91 base metal (blue) is then adjusted to obtain the true stress-strain relationship for the G91 weld metal (red). This adjustment is made using a hardness ratio (260 HV / 220 HV) of G91 weld metal over G91 base metal (see Fig. 9e).

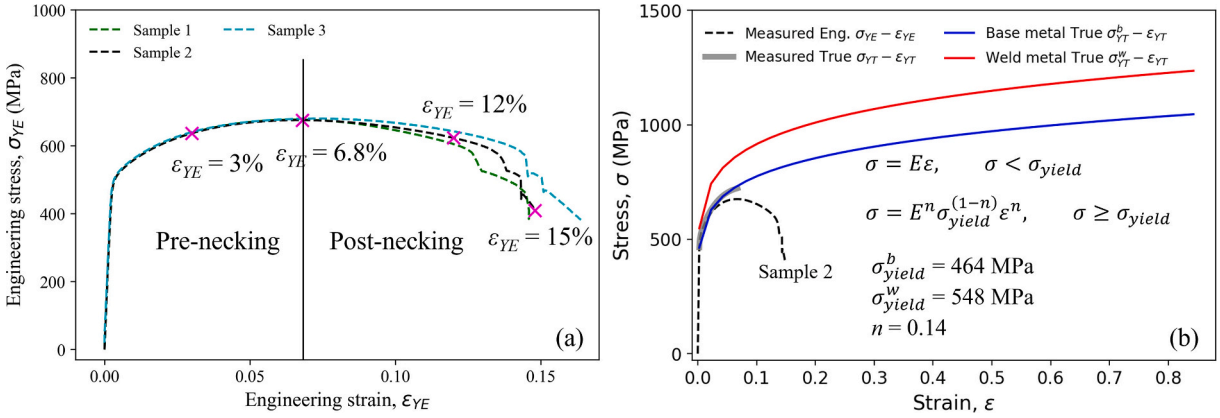

Fig. A.1. (a) Engineering stress-strain curves for G91/C22 cross-weld samples by uniaxial tensile testing at room temperature. (b) Estimation of the true stress-strain relationships for G91 base and weld metal. The post-necking behavior is approximated by fitting the pre-necking portion with the Hollomon relation.

Appendix B

To explain the high triaxiality factor at the bonding interface, the characteristic stresses, such as maximum (σ_1), intermediate (σ_2), minimum (σ_3) principal stresses, and von Mises stress (σ_v) were extracted at four monitoring positions for the case with the residual stress from welding and PWHT. Those four positions are indicated in Fig. 13a and the bottom inset picture of Fig. B.1.

Fig. B.1a shows the stress evolution of an interface element (mc) on the C22 clad side during tensile loading. The initial stress is the residual stress from welding and PWHT, and thus the stress state is non-uniaxial, resulting in TF = 2.2. As tensile loading advances, the stress state transitions to a uniaxial tensile state with TF = 1.0. Fig. B.1b-c show the stress evolution at the top and bottom of an interface element on the substrate side, respectively. Both positions exhibit non-uniaxial stress states initially due to the residual stress, with a significant stress gradient between them. Specifically, at the top of the element (mst), the stresses ($\sigma_1 = 205$ MPa, $\sigma_2 = 168$ MPa, $\sigma_3 = 6$ MPa, and $\sigma_v = 183$ MPa) result in TF = 2.1, while at the bottom of the element (msb), the stresses ($\sigma_1 = 7$ MPa, $\sigma_2 = -159$ MPa, $\sigma_3 = -170$ MPa, and $\sigma_v = 171$ MPa) result in TF = −1.9. During subsequent loading, the residual stress is compounded with the applied load, resulting in a monotonic increase in σ_1. However, the non-uniaxial stress state is maintained for both positions, and consequently TF does not become 1.0. Fig. B.1d shows the stress evolution of an element in the interior of the G91 substrate (msi), exhibiting a similar transition from non-uniaxial to uniaxial tensile state to that in Fig. B.1a as loading progresses. Comparing results among these monitoring locations indicates the significant role of stress gradient in preventing the stress state from transitioning to a uniaxial tensile state.

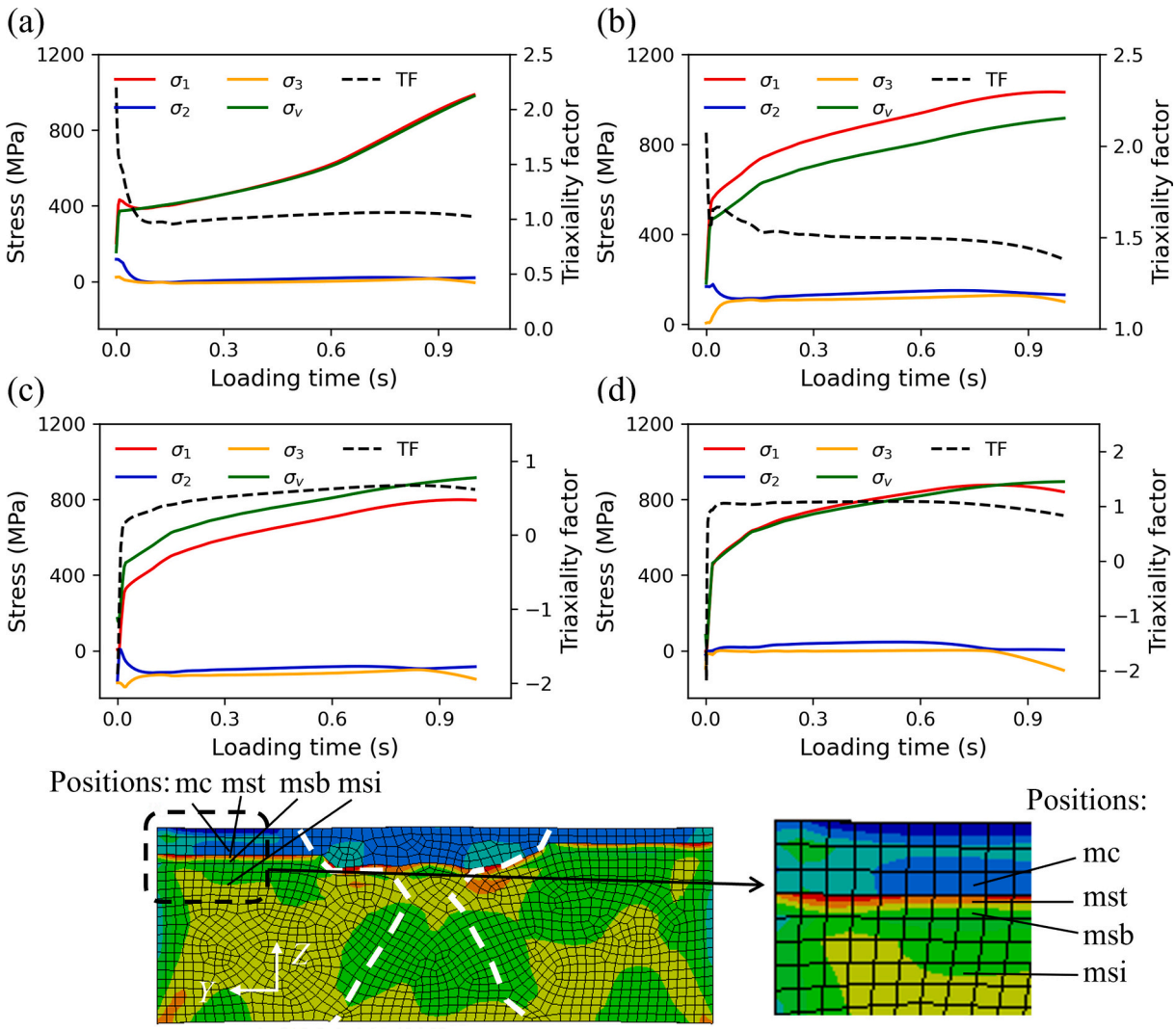

Fig. B.1. Evolution of maximum, intermediate, minimum principal stresses, von Mises stress and triaxiality factor at four monitoring points, (a) mc, (b) mst, (c) msb, and (d) msi for the tensile model incorporating residual stress from welding and PWHT. The location of these points is indicated in the bottom inset and Fig. 13a. Specifically, Point mc is in an interface element on the C22 clad side, Points mst and msb in an interface element on the G91 substrate side, and Point msi in an interior element of the substrate. Points mst and msb are at the top and bottom of the interface element, respectively, capturing the presence of a significant local stress gradient.

Correspondingly, Fig. B.2 shows the evolution of σ_1, σ_2, σ_3, σ_v, and TF during tensile loading for the case without considering the residual stress from welding and PWHT. The monitoring positions are placed in the same elements as those in Fig. B.1, with their exact locations indicated in the bottom-right inset and Fig. 13b. As shown in this figure, the stress state at these positions remains in a uniaxial tensile state throughout the tensile loading process, resulting in TF = 1.0.

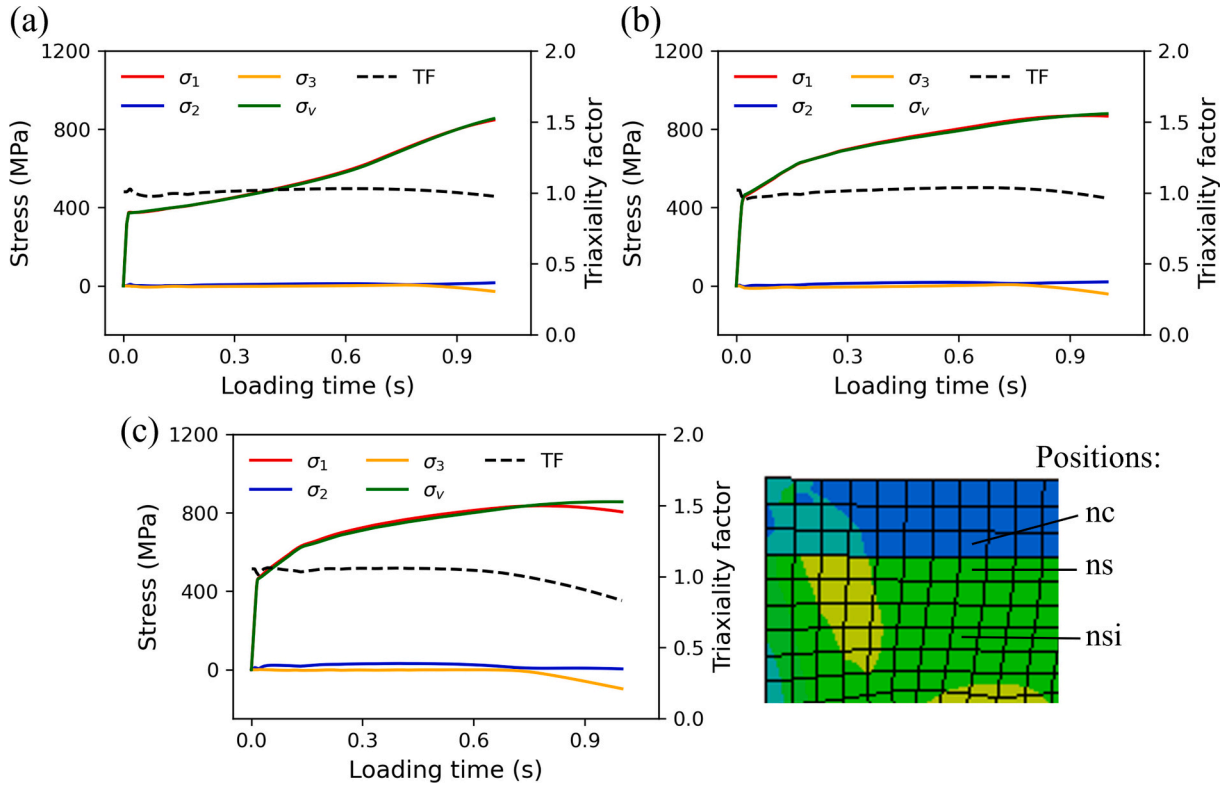

Fig. B.2. Evolution of maximum, intermediate, minimum principal stresses, von Mises stress and triaxiality factor at three monitoring points, (a) nc, (b) ns, and (c) nsi for the tensile model without considering residual stress. The location of these points is indicated in the bottom-right inset and Fig. 13b. Specifically, Point nc is in an interface element on the clad side, Point ns in an interface element on the substrate side, and Point nsi in an interior element of the substrate.

Appendix C. Supplementary data

Supplementary data to this article can be found online at https://doi.org/10.1016/j.jmapro.2024.05.036.

References

[1] Bhanu V, Gupta A, Pandey C. Investigation on joining P91 steel and Incoloy 800HT through gas tungsten arc welding for Advanced Ultra Super Critical (AUSC) power plants. J Manuf Process 2022;80:558–80. https://doi.org/10.1016/j.jmapro.2022.06.029.

[2] Sirohi S, Pandey C, Goyal A. Role of the Ni-based filler (IN625) and heat-treatment on the mechanical performance of the GTA welded dissimilar joint of P91 and SS304H steel. J Manuf Process 2021;65:174–89. https://doi.org/10.1016/j.jmapro.2021.03.029.

[3] Thakare JG, Pandey C, Mahapatra MM, Mulik RS. An assessment for mechanical and microstructure behavior of dissimilar material welded joint between nuclear grade martensitic P91 and austenitic SS304 L steel. J Manuf Process 2019;48:249–59. https://doi.org/10.1016/j.jmapro.2019.10.002.

[4] Rybalka KV, Beketaeva LA, Davydov AD. Effect of self-passivation on the electrochemical and corrosion behaviour of alloy C-22 in NaCl solutions. Corros Sci 2012;54:161–6. https://doi.org/10.1016/j.corsci.2011.09.009.

[5] Ban H, Zhu J, Shi G. Cyclic loading tests on welded connections of stainless-clad bimetallic steel and modelling. J Constr Steel Res 2020;171:106140. https://doi.org/10.1016/j.jcsr.2020.106140.

[6] Chen J, Li J, Nie S, Tang M, Yu X, Elchalakani M. Experimental and finite-element study on cyclic tensile properties of stainless-clad bimetallic steel plate. J Mater Civ Eng 2021:33. https://doi.org/10.1061/(asce)mt.1943-5533.0003966.

[7] Li H, Zhang L, Zhang B, Zhang Q. Interfacial fracture behavior of a stainless/carbon steel bimetal plate in a uniaxial tension test. Results Phys 2019;14:102470. https://doi.org/10.1016/j.rinp.2019.102470.

[8] Ban H, Yang X, Hai L, Shi Y. Low-cycle fatigue behaviour and fracture feature of stainless-clad bimetallic steel. J Constr Steel Res 2022;196:107437. https://doi.org/10.1016/j.jcsr.2022.107437.

[9] Hua J, Wang F, Huang L, Wang N, Xue X. Experimental study on mechanical properties of corroded stainless-clad bimetallic steel bars. Construct Build Mater 2021;287:123019. https://doi.org/10.1016/j.conbuildmat.2021.123019.

[10] Tang M, Li J, Yu X, Nie S. Tensile behavior of stainless steel clad plates with different cladding ratios. J Constr Steel Res 2021;182:106641. https://doi.org/10.1016/j.jcsr.2021.106641.

[11] Suman S, Biswas P. Finite element analysis of in- process thermal mitigation of welding induced residual stresses in 9Cr-1Mo-V steel butt joint considering phase transformation. J Manuf Process 2021;70:361–75. https://doi.org/10.1016/j.jmapro.2021.08.027.

[12] Sabzi M, Dezfuli SM. Post weld heat treatment of hypereutectoid hadfield steel: characterization and control of microstructure, phase equilibrium, mechanical properties and fracture mode of welding joint. J Manuf Process 2018;34:313–28. https://doi.org/10.1016/j.jmapro.2018.06.009.

[13] Ramkumar KD, Krishnan SR, Ramanand R, Logesh S, Satyandas T, Ameer A, et al. Structure-property relationships of PCGTA welds of Inconel X750 in as-welded and post-weld heat treated conditions - a comparative study. J Manuf Process 2015;20:1–14. https://doi.org/10.1016/j.jmapro.2015.10.003.

[14] Cattivelli A, Roy MJ, Burke MG, Dhers J, Lee TL, Francis JA. Internal stresses in a clad pressure vessel steel during post weld heat treatment and their relevance to underclad cracking. Int J Press Vessel Pip 2021;193:104448. https://doi.org/10.1016/j.ijpvp.2021.104448.

[15] Makoto U, Jinya K, Hiroyuki N, Kunio O. Evaluation of residual stress near the weld overlay cladding by welding and post-weld heat treatment. Weld Int 2014;28:521–34. https://doi.org/10.1080/09507116.2012.753238.

[16] Wang L, Wu D, Cui C, Wen P, Xu M, Zhou P, et al. In situ observation on fracture behavior of the three-phase zone of the L415/N08825 bimetallic composite pipe welded joint. Eng Fract Mech 2022;276:108898. https://doi.org/10.1016/j.engfracmech.2022.108898.

[17] Hamilton JD, Sorondo S, Li B, Qin H, Rivero IV. Mechanical behavior of bimetallic stainless steel and gray cast iron repairs via directed energy deposition additive manufacturing. J Manuf Process 2023;85:1197–207. https://doi.org/10.1016/j.jmapro.2022.12.029.

[18] Tavassolimanesh A, Alavi Nia A. A new approach for manufacturing copper-clad aluminum bimetallic tubes by friction stir welding (FSW). J Manuf Process 2017;30:374–84. https://doi.org/10.1016/j.jmapro.2017.10.010.

[19] Gou NN, Zhang JX, Zhang LJ, Li ZG, Bi ZY. Single pass fiber laser butt welding of explosively welded 2205/X65 bimetallic sheets and study on the properties of the welded joint. Int J Adv Manuf Technol 2016;86:2539–49. https://doi.org/10.1007/s00170-015-8335-0.

[20] Gou NN, Zhang JX, Wang JL, Bi ZY. Butt welding of 2205/X65 bimetallic sheet and study on the inhomogeneity of the properties of the welded joint. J Mater Eng Perform 2017;26:1801–7. https://doi.org/10.1007/s11665-017-2549-2.
[21] Ye C, Lu G, Liu Q, Ni L, Wei X, Fang X. Microstructure and mechanical properties of 10CrNi3MoV steel-SS304L composite bimetallic plates butt joint by shielded metal arc welding. J Mater Eng Perform 2021;30:2047–56. https://doi.org/10.1007/s11665-021-05477-x.
[22] Dhib Z, Guermazi N, Gaspérini M, Haddar N. Cladding of low-carbon steel to austenitic stainless steel by hot-roll bonding: microstructure and mechanical properties before and after welding. Mater Sci Eng A 2016;656:130–41. https://doi.org/10.1016/j.msea.2015.12.088.
[23] Liying L, Jun X, Bin H, Xiaolei W. Microstructure and mechanical properties of welded joints of L415/316L bimetal composite pipe using post internal-welding process. Int J Press Vessel Pip 2020;179:104026. https://doi.org/10.1016/j.ijpvp.2019.104026.
[24] Chen X, Inao D, Tanaka S, Mori A, Li X, Hokamoto K. Explosive welding of Al alloys and high strength duplex stainless steel by controlling energetic conditions. J Manuf Process 2020;58:1318–33. https://doi.org/10.1016/j.jmapro.2020.09.037.
[25] Deng D, Kiyoshima S, Ogawa K, Yanagida N, Saito K. Predicting welding residual stresses in a dissimilar metal girth welded pipe using 3D finite element model with a simplified heat source. Nucl Eng Des 2011;241:46–54. https://doi.org/10.1016/j.nucengdes.2010.11.010.
[26] Deng D, Ogawa K, Kiyoshima S, Yanagida N, Saito K. Prediction of residual stresses in a dissimilar metal welded pipe with considering cladding, buttering and post weld heat treatment. Comput Mater Sci 2009;47:398–408. https://doi.org/10.1016/j.commatsci.2009.09.001.
[27] Zhang W, Kim CH, DebRoy T. Heat and fluid flow in complex joints during gas metal arc welding - part I: numerical model of fillet welding. J Appl Phys 2004;95:5210–9. https://doi.org/10.1063/1.1699485.
[28] Deng D, Murakawa H. Prediction of welding residual stress in multi-pass butt-welded modified 9Cr-1Mo steel pipe considering phase transformation effects. Comput Mater Sci 2006;37:209–19. https://doi.org/10.1016/j.commatsci.2005.06.010.
[29] Yaghi AH, Hyde TH, Becker AA, Sun W. Finite element simulation of welding and residual stresses in a P91 steel pipe incorporating solid-state phase transformation and post-weld heat treatment. J Strain Anal Eng Des 2008;43:275–93. https://doi.org/10.1243/03093247JSA372.
[30] Li S, Li J, Sun G, Deng D. Modeling of welding residual stress in a dissimilar metal butt-welded joint between P92 ferritic steel and SUS304 austenitic stainless steel. J Mater Res Technol 2023;23:4938–54. https://doi.org/10.1016/j.jmrt.2023.02.123.
[31] Pandey C, Mahapatra MM. Effect of heat treatment on microstructure and hot impact toughness of various zones of P91 welded pipes. J Mater Eng Perform 2016;25:2195–210. https://doi.org/10.1007/s11665-016-2064-x.
[32] Yaghi AH, Hyde TH, Becker AA, Sun W. Finite element simulation of welding and residual stresses in a P91 steel pipe incorporating solid-state phase transformation and post-weld heat treatment. J Strain Anal Eng Des 2008;43:275–93. https://doi.org/10.1243/03093247JSA372.
[33] Edmonds DV, He K, Rizzo FC, De Cooman BC, Matlock DK, Speer JG. Quenching and partitioning martensite-a novel steel heat treatment. Mater Sci Eng A 2006;438–440:25–34. https://doi.org/10.1016/j.msea.2006.02.133.
[34] Yaghi AH, Hyde TH, Becker AA, Sun W, Wen W, Hilson G, et al. Comparison of measured and modelled residual stresses in a welded P91 steel pipe undergoing post weld heat treatment. Int J Press Vessel Pip 2020;181:104076. https://doi.org/10.1016/j.ijpvp.2020.104076.
[35] Yaghi AH, Hyde TH, Becker AA, Sun W. Finite element simulation of welded P91 steel pipe undergoing post-weld heat treatment. Sci Technol Weld Join 2011;16:232–8. https://doi.org/10.1179/1362171810Y.0000000018.
[36] Pandey C, Mahapatra MM, Kumar P, Saini N. Some studies on P91 steel and their weldments. J Alloys Compd 2018;743:332–64. https://doi.org/10.1016/j.jallcom.2018.01.120.
[37] Zhang Z, Ge P, Zhao GZ. Numerical studies of post weld heat treatment on residual stresses in welded impeller. Int J Press Vessel Pip 2017;153:1–14. https://doi.org/10.1016/j.ijpvp.2017.05.005.
[38] Kiranmayi AV. Characterising high energy beam welding in structural steels with numerical simulation and validation. Doctoral dissertation,. University of Bristol; 2015.
[39] Jiang W, Yang B, Gong JM, Tu ST. Effects of clad and base metal thickness on residual stress in the repair weld of a stainless steel clad plate. J Press Vessel Technol Trans ASME 2011;133:1–9. https://doi.org/10.1115/1.4004565.
[40] Qiao D, Feng Z, Zhang W, Wang Y, Crooker P. MODELING OF WELD RESIDUAL PLASTIC STRAIN AND STRESS IN DISSIMAILAR METAL BUTT WELD IN NUCLEAR REACTORS. Proc. ASME 2013 Press. Vessel. Pip. Div. Conf. 2013. p. 1–8.
[41] Haynes International. https://haynesintl.com/alloys/alloy-portfolio_/Corrosion-resistant-Alloys/HASTELLOY-C-22. https://haynesintl.com/alloys/alloy-portfolio_/Corrosion-resistant-Alloys/HASTELLOY-C-22; 2019. n.d.
[42] ABAQUS Analysis User''s Manual. Dassault Systémes Simulia Corp, Providence, RI, USA. 2019.
[43] Payton TK. On the improvement of creep-fatigue behavior of grade 91 weldments. Master dissertation,. The Ohio State University; 2017.
[44] Gao X, Okigami F, Avedissian N, Zhang W. An experimental and modeling study on warping in additively manufactured overhang structures. Addit Manuf 2024;81:104017. https://doi.org/10.1016/j.addma.2024.104017.
[45] Jiang W, Luo Y, Zeng Q, Wang J, Tu ST. Residual stresses evolution during strip clad welding, post welding heat treatment and repair welding for a large pressure vessel. Int J Press Vessel Pip 2021;189:104259. https://doi.org/10.1016/j.ijpvp.2020.104259.
[46] Pandey C, Mahapatra MM. Effect of groove design and post-weld heat treatment on microstructure and mechanical properties of P91 steel weld. J Mater Eng Perform 2016;25:2761–75. https://doi.org/10.1007/s11665-016-2127-z.
[47] Wang Y, Kannan R, Li L. Identification and characterization of Intercritical heat-affected zone in as-welded grade 91 weldment. Metall Mater Trans A Phys Metall Mater Sci 2016;47:5680–4. https://doi.org/10.1007/s11661-016-3736-8.
[48] Laha K, Chandravathi KS, Parameswaran P, Rao KBS, Mannan SL. Characterization of microstructures across the heat-affected zone of the modified 9Cr-1Mo weld joint to understand its role in promoting type IV cracking. Metall Mater Trans A Phys Metall Mater Sci 2007;38:58–68. https://doi.org/10.1007/s11661-006-9050-0.
[49] Davis EA, Connelly FM. Stress distribution and plastic deformation in rotating cylinders of strain-hardening material. J Appl Mech 1959;26:25–30. https://doi.org/10.1115/1.4011918.
[50] Mirza MS, Barton DC, Church P. The effect of stress triaxiality and strain-rate on the fracture characteristics of ductile metals. J Mater Sci 1996;31:453–61. https://doi.org/10.1007/BF01139164.
[51] Akbari Mousavi SAA, Al-Hassani STS, Atkins AG. Bond strength of explosively welded specimens. Mater Des 2008;29:1334–52. https://doi.org/10.1016/j.matdes.2007.06.010.
[52] Findik F. Recent developments in explosive welding. Mater Des 2011;32:1081–93. https://doi.org/10.1016/j.matdes.2010.10.017.